

Viscous fingering in fractured porous media

Runar L. Berge^{*1}, Inga Berre^{1,2}, Eirik Keilegavlen¹, and Jan M. Nordbotten¹

¹Department of Mathematics, University of Bergen, Bergen, Norway

²NORCE, Bergen, Norway

June 26, 2019

Abstract

The effect of heterogeneities induced by highly permeable fracture networks on viscous miscible fingering in porous media is examined using high-resolution numerical simulations. We consider the planar injection of a less viscous fluid into a two-dimensional fractured porous medium which is saturated with a more viscous fluid. This problem contains two sets of fundamentally different preferential flow regimes; the first is caused by the viscous fingering and the second is due to the permeability contrasts between the fractures and rock matrix. We study the transition from a regime where the flow is dominated by the viscous instabilities, to a regime where the heterogeneities induced by the fractures define the flow paths. We find that fractures greatly affect the viscous fingering, even for small permeability differences between the rock matrix and the fractures. The interaction between the viscosity contrast and permeability contrast causes channeling of the less viscous fluid through the fractures and back to the rock. This channeling stabilizes the displacement front in the rock matrix, and the viscous fingering ceases for the higher permeability contrast. Several different fracture geometries are considered, and we observe a complex interplay between the geometries and unstable flow. While we find that the most important dimensionless number determining the effect of the fracture network is a weighted ratio of the permeability of the fractures and the permeability of the rock matrix, the exact point for the cross-over regime is highly dependent on the geometry of the fracture network.

1 Introduction

Viscous fingering in a porous medium is a fundamental process occurring within a wide range of flow processes, including for CO₂ storage, enhanced oil recovery, and geothermal energy systems. The porous rocks that are relevant for these applications have often undergone fracturing processes, and fractures do in general span the entire reservoir [6]. The fractures enforce a structural constraint on fluid flow and transport through the domain, and this paper targets the interplay between unstable miscible fingering and channeling through fractures that are more permeable than the surrounding rock matrix.

When a less viscous fluid displaces a more viscous fluid, hydrodynamical instabilities are induced that may cause viscous fingering [19]. Miscible viscous fingering in a homogeneous medium has been extensively studied by a variety of different methods, including linear stability analysis [41, 42], numerical simulations [29, 44, 45, 8], and laboratory experiments [23, 3, 33, 9]. These studies have characterized the evolution of the viscous fingering from the initialization to the later stages. The onset of viscous fingers can be predicted by the wave number with the highest growth rate from linear stability analysis. As the instabilities grow, the flow is governed by different mechanisms such as splitting, merging, or shielding [19]. The exact behavior of the displacement front is determined by the parameter regime, and the viscous instabilities depend on a wide range of factors, including gravity [24], miscibility [17], anisotropic dispersion [43], mixing [20], and reactions [10].

Porous media found in geological formations are in general not homogeneous, but vary on a wide range of length scales, from the pore scale to the reservoir scale. De Wit and Homsy [11, 12] and Nicolaidis et al. [28] considered different randomly varying permeability fields and found that the preferential flow paths given by the permeability field are competing with the unstable flow paths from the viscous fingering. More structured permeability fields have also been studied, with the main focus on layered porous media. When the flow is predominantly aligned with the permeable layers, the heterogeneities tend to cause channeling through the domain [30, 38, 39].

When fractures are present in a porous medium, the fractures can act as preferential flow paths due to high permeability contrasts with the rock matrix. Fractures can give rise to complicated flow and transport patterns

*Corresponding Author: runar.berge@uib.no

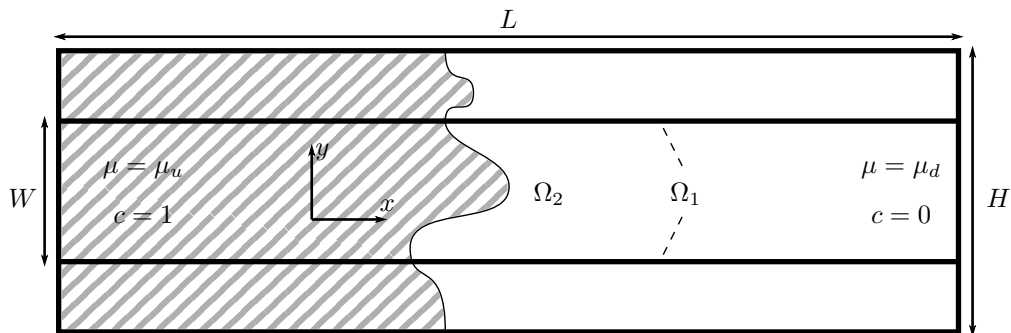


Figure 1: A domain of length L and width H . The rock matrix is denoted by Ω_2 and contains two fractures denoted Ω_1 . The distance between the fractures is given by W . The porous medium is initially filled by a fluid of viscosity μ_d and displaced by a fluid of viscosity μ_u .

through a porous medium, and they present challenges to modeling [27], upscaling [31], and discretization [16], which are further complicated by fracture geometries [5]. These challenges have received considerable attention the last two decades; for an overview, we refer the reader to the textbooks by Dietrich et al. [13] and Sahimi [37], and the review study by Berre et al. [7] on different mathematical models of fracture flow. A popular class of conceptual models for fractured porous medium is the discrete-fracture-matrix (DFM) models, where flow and transport in the fractures are explicitly represented. An efficient approach of representing DFM models is to consider fractures as lower-dimensional inclusions in the rock matrix due to their large aspect ratios [25, 21]. This approach has led to the development of accompanying discretization strategies; see, e.g., [32, 34, 40, 16].

Despite the extensive work on both viscous fingering and flow in fractures, little to no attention has been given to characterize the interaction between the viscous instabilities and preferential flow paths through a fracture network. This paper fills this gap, by addressing three key questions: (i) how large must the permeability contrasts between the fractures and rock matrix be to effect the viscous instabilities, (ii) how does the interplay between the viscous instabilities and fractures effect the flow patters, and (iii) how does different fracture geometries affect the answer to question (i) and (ii). To answer these questions, we exploit the recent advances within modeling and simulation tools that focus on flow and transport in fractured porous media. We employ a DFM model, and by state-of-the-art numerical simulations characterize unstable miscible displacement through different fracture network geometries. The fractured porous media considered have fracture density and length scales similar to the viscous finger width and domain size.

The remaining manuscript is laid out as follows. In section 2, we present the governing equations for miscible viscous flow in a fractured porous media. Special attention is given to the mixed-dimensional DFM model. In section 2.2, the equations are represented in dimensionless form, and we discuss the two new dimensionless numbers that appear due to the fractures. In section 3, we briefly discuss the numerical method. The results given in section 4 are divided into four subsection, one for each fracture geometry considered, and one subsection dedicated to comparing the flow paths through the different geometries. Finally, we give concluding remarks.

2 Governing equations

A schematic of the problem geometry is shown in figure 1. We consider two incompressible fluids with different viscosities $\mu_u \leq \mu_d$, in a periodic fractured porous media. The two fluids are completely miscible and can therefore be modeled as a single-phase fluid with two components. The fractures, denoted by Ω_1 , are considered as one-dimensional (1d) inclusions, embedded in a surrounding two-dimensional (2d) rock matrix denoted by Ω_2 . Throughout this work we use subscripts “1” and “2” when it is necessary to distinguish fracture and rock matrix values, respectively. The fluid follows Darcy’s law both in the rock matrix and in the fractures. The rock matrix and fractures have constant, but different, scalar permeabilities k_1 and k_2 , respectively. The porosity ϕ is constant, and the diffusivity, D , is assumed isotropic and independent of the component concentration. The viscosity of the mixed fluid depends exponentially on the mass ratio, c , of the two components, $\mu = \mu_d e^{-Rc}$, with $R = \ln \mu_d / \mu_u$. The governing equations in the rock matrix domain Ω_2 are given by

$$\begin{aligned} \mathbf{u}_2 &= -\frac{k_2}{\mu(c)} \nabla p_2, \quad \nabla \cdot \mathbf{u}_2 = 0 \\ \phi \frac{\partial c}{\partial t} + \nabla \cdot (c \mathbf{u}_2 - D \nabla c) &= 0 \end{aligned} \quad \text{in } \Omega_2, \quad (1)$$

in addition to the boundary conditions.

The fractures define an internal boundary $\Gamma_1 = \{\Gamma^+, \Gamma^-\}$ (each fracture has two interfaces with the rock matrix) of the rock matrix. The interaction between the fractures and the rock matrix is given by the coupling variables λ_u and λ_c . They represent the fluid flux and diffusive flux from the rock matrix to the fractures, respectively. In the rock matrix domain, Ω_2 , these fluxes appear as Neuman-type boundary conditions

$$\mathbf{u}_2 \cdot \mathbf{n} = \lambda_u, \quad -D\nabla c \cdot \mathbf{n} = \lambda_c \quad \text{on } \Gamma_1, \quad (2)$$

where \mathbf{n} is the normal vector pointing from the rock matrix to the fracture.

Following Nordbotten et al. [32], the fractures are modeled as lower-dimensional manifolds. An aperture, a , is associated with the fractures. The coupling terms λ_i , $i \in \{u, c\}$ are defined on the positive and negative fracture sides Γ^+ and Γ^- by superscripts λ_i^+ and λ_i^- , and the jump operator is defined as

$$[[\lambda_i]] = \lambda_i^+ + \lambda_i^-.$$

The governing equations in the fracture domain, Ω_1 , are written as

$$\begin{aligned} \mathbf{u}_1 &= -\frac{k_1}{\mu(c)} \nabla p_1, \quad \nabla \cdot \mathbf{u}_1 - [[\lambda_u]] = 0 \\ \frac{\partial \phi_{ac}}{\partial t} + \nabla \cdot (c\mathbf{u}_1 - Da\nabla c) - [c\lambda_u] - [[\lambda_c]] &= 0 \end{aligned} \quad \text{in } \Omega_1. \quad (3)$$

The diffusivity in the rock matrix is in general different from the diffusivity in the fractures. We have here made the simplification that the diffusivity in the fractures is the product of the matrix diffusivity and the fracture aperture. This choice results in a diffusive front that, in the absence of advection, is the same in both fractures and rock matrix.

Two extra terms $[[\lambda_u]]$ and $[[\lambda_c]]$ appear in the conservation laws in equation (3). The first term represents the inflow and outflow fluid flux from the rock matrix to the fractures. The second term represents the diffusion between the two domains. The units of equation (3) are discussed in detail in section 2.2, but for now, note that the equations are scaled by a length factor compared to the rock matrix equation (1).

To close the system of equations constitutive laws for the coupling fluxes are needed. We define a Darcy type relation for the flux between the rock matrix and the lower-dimensional fractures (see, e.g., Martin et al. [25]):

$$\lambda_u = -\frac{k_1}{a\mu(c)} \frac{p_1 - \text{tr}(p_2)}{a/2}, \quad \lambda_c = -D \frac{c_1 - \text{tr}(c_2)}{a/2}, \quad (4)$$

where $\text{tr}(\cdot)$ is the trace operator.

The intersection of two or more fractures is a 0d point, where we enforce pressure and flux continuity of fluid and mass transport for all fractures that intersect in this point. For intersecting fractures that have the same permeability, this is usually a reasonable choice (see, e.g., Stefansson et al. [40]).

2.1 Boundary and initial conditions

We consider flow that is periodic in the y -direction:

$$\begin{aligned} p_d(x, 0, t) &= p_d(x, H, t), & \mathbf{u}_d(x, 0, t) &= \mathbf{u}_d(x, H, t), \\ c(x, 0, t) &= c(x, H, t), & D\nabla c(x, 0, t) &= D\nabla c(x, H, t), \end{aligned}$$

for $d = 1, 2$. A constant flux, U_2 , is enforced at the upstream boundary of the rock matrix boundary:

$$\mathbf{u}_2(0, y, t) \cdot \mathbf{n} = -U_2 \quad (0, y) \in \partial\Omega_2, \quad (5)$$

where \mathbf{n} is the outer normal vector. The upstream flux on the fracture boundary,

$$\mathbf{u}_1(0, y, t) \cdot \mathbf{n} = U_1 = \frac{k_1}{k_2} U_2 \quad (0, y) \in \partial\Omega_1, \quad (6)$$

is chosen such that the initial pressure drop (almost) only varies in the x -direction. A fixed pressure is given at the downstream boundary:

$$p_d(L, y, t) = 0 \quad [L, y] \in \partial\Omega_d.$$

The initial condition is given by a step jump in concentration

$$c(x, y, t = 0) = \begin{cases} 1 - 0.05e(x, y) & x < S \\ 0 & x \geq S, \end{cases}$$

where $e(x, y) \in [0, 1]$ is a uniformly random perturbation added to initialize the viscous instabilities. The parameter $S \in [0, L]$ gives the position of the concentration jump. If $S = 0$ the perturbation is given to the

upstream concentration boundary condition, $c(0, y, t) = 1 - e(0, y)$. It is well known that the onset time of the nonlinear viscous fingering is very sensitive to the amplitude and type of perturbation [15]. While our choice of perturbation initially has a grid dependence, the shortest wavelength introduced by the grid is significantly shorter than the first unstable mode from the linear stability analysis and therefore decay quickly until the onset of the nonlinear viscous fingering. If the onset time of the unstable viscous fingering is of interest, more care is needed. Possible techniques to address this issue can be found in, e.g., the papers by Riaz et al. [35] and Elenius and Johannsen [14].

2.2 Scaling analysis

The characteristic length scale for our problem is given by the vertical separation of the fractures W . The characteristic flux is chosen as the matrix injection flux U_2 , while the characteristic viscosity is μ_d . By following classical results from viscous fingering (see, e.g., Tan and Homsy [41]), the Peclét number is defined by $Pe = \frac{U_2 W}{D}$, the characteristic time by $T = \frac{\phi W}{U_2}$, and the characteristic pressure by $P = \frac{\mu_d U_2 W}{k_2}$. The dimensionless variables are denoted by a hat $\hat{\cdot}$, which by a rescaling of equation 1 gives the dimensionless equations defined in the rock matrix:

$$\begin{aligned} \hat{\mathbf{u}}_2 &= -\frac{1}{\hat{\mu}(c)} \nabla \hat{p}_2, & \nabla \cdot \hat{\mathbf{u}}_2 &= 0 \\ & & & \text{in } \hat{\Omega}_2. \end{aligned} \quad (7)$$

$$\mathcal{A} \frac{\partial c}{\partial \hat{t}} + \nabla \cdot c \hat{\mathbf{u}}_2 - \frac{1}{Pe} \Delta c = 0$$

Note that for our choice of dimensionless numbers, the characteristic width of the viscous fingers (as the length scale that enters into the Peclét number) coincide with the vertical separation of the fractures W .

The non-dimensionalization of the variables in the fractures needs some more care. The fluid flux is defined as volumetric rate per area, which in the 1d fractures is given by units $[\mathbf{u}_1] = \text{m}^2/\text{s}$, as opposed to the rock matrix flux $[\mathbf{u}_2] = (\text{m}^2/\text{s})/\text{m} = \text{m}/\text{s}$. Thus, the flux \mathbf{u}_2 and permeability $[k_1] = \text{m}^3$ in the fractures are scaled by an extra length scale compared to the parameters in the rock matrix. The permeability in the fractures is typically proportional to the fracture aperture [25].

We define the dimensionless 1d fracture flux as $\hat{\mathbf{u}}_1 = \frac{1}{W U_2} \mathbf{u}_1$, and the dimensionless coupling fluxes by $\hat{\lambda}_u = \frac{1}{U_2} \lambda_u$, and $\hat{\lambda}_d = \frac{W}{D} \lambda_c$. From the boundary conditions defined in section 2.1, we obtain the same characteristic pressure in the fractures as in the rock matrix $P = \frac{\mu_d U_2 W}{k_2}$. Rescaling equation (3), we get the dimensionless equations:

$$\begin{aligned} \hat{\mathbf{u}}_1 &= -\frac{\mathcal{K}}{\hat{\mu}(c)} \nabla \hat{p}, & \nabla \cdot \hat{\mathbf{u}} - \llbracket \hat{\lambda}_u \rrbracket &= 0 \\ & & & \text{in } \hat{\Omega}_1, \end{aligned} \quad (8)$$

$$\mathcal{A} \frac{\partial c}{\partial \hat{t}} + \left(\nabla \cdot c \hat{\mathbf{u}} - \llbracket c \hat{\lambda}_u \rrbracket \right) - \frac{1}{Pe} \left(\mathcal{A} \Delta c + \llbracket \hat{\lambda}_c \rrbracket \right) = 0$$

where we have defined the dimensionless numbers

$$\mathcal{K} = \frac{k_1}{W k_2}, \quad \mathcal{A} = \frac{a}{W}. \quad (9)$$

Recall that the permeability in the fractures has units m^3 , so the weighted permeability ratio \mathcal{K} , is in fact dimensionless. The dimensionless number \mathcal{A} gives the relative fracture aperture compared to the rock matrix domain. The dimensionless coupling equations are obtained by rescaling equation (4):

$$\hat{\lambda}_u = -\frac{\mathcal{K}}{\mathcal{A}^2} \frac{\hat{p}_1 - \text{tr}(\hat{p}_2)}{\hat{\mu}(c)/2}, \quad \hat{\lambda}_c = -\frac{1}{\mathcal{A}} \frac{c_1 - \text{tr}(c_2)}{1/2}. \quad (10)$$

To better understand some of the phenomena in the later result section, it is beneficial to point out a few key-relationships between the dimensionless numbers \mathcal{K} and \mathcal{A} , and how they relate to problem setup. From the boundary condition given in equations (5) and (6) we note that the weighted permeability ratio is equal to the volumetric flux ratio at the upstream boundary, i.e., $\mathcal{K} = \frac{U_1}{U_2 W}$. If we only consider advection, we can see from equations (7) and (8) that the advection in the fractures is scaled by the ratio \mathcal{K}/\mathcal{A} . This means that when the weighted permeability ratio is equal the width ratio, $\mathcal{K} = \mathcal{A}$, the velocity of the advection in the rock matrix is approximately equal to the velocity of the advection in the fractures (up to any velocity differences induced by viscous fingering). When the weighted permeability ratio is larger than the width ratio, $\mathcal{K} > \mathcal{A}$, the advection in the fractures is faster than the advection in the rock matrix.

To summarize, the dimensionless variables are

$$\begin{aligned} \hat{\mathbf{x}} &= \frac{1}{W} \mathbf{x}, & \hat{t} &= \frac{U_2}{\phi W} t, & \hat{\mathbf{u}}_2 &= \frac{1}{U_2} \mathbf{u}_2, \\ \hat{\mathbf{u}}_1 &= \frac{1}{W U_2} \mathbf{u}_1, & \hat{p}_2 &= \frac{k_2}{\mu_d U_2 W} p_2, & \hat{p}_1 &= \frac{k_2}{\mu_d U_2 W} p_1, \\ \hat{\lambda}_u &= \frac{1}{U_2} \lambda_u, & \hat{\lambda}_c &= \frac{W}{D} \lambda_c, & \hat{\mu} &= \frac{1}{\mu_d} \mu. \end{aligned}$$

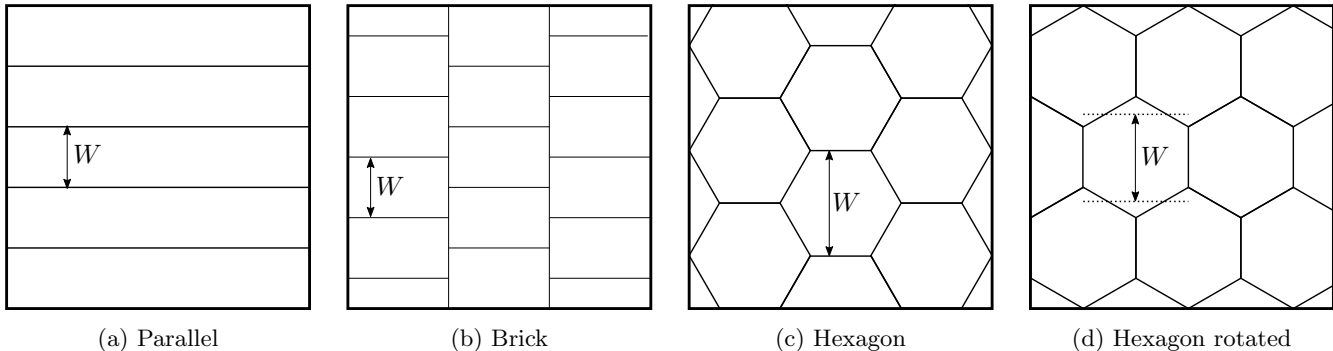


Figure 2: Schematics of the fracture networks used in the simulations. The characteristic width W is indicated by the double arrow. The principle direction of flow is from left to right. The hexagon fractures (c) and rotated hexagon networks (d) represent the same fracture geometry and are equivalent up to a rotation, but we refer to them as two different networks as the network is anisotropic, and flow will differ in the two directions anisotropy.

From the dimensionless equations (7)-(10), we obtain that the dimensionless numbers governing the behavior of this system are:

$$Pe = \frac{U_2 W}{D}, \quad R = \ln\left(\frac{\mu_d}{\mu_u}\right), \quad \mathcal{K} = \frac{k_1}{W k_2}, \quad \mathcal{A} = \frac{a}{W}. \quad (11)$$

3 Numerical method

The elliptic equation for fluid pressure in equations (7) and (8) is discretized by the multi-point flux approximation method [1]. This is a consistent, mass conservative finite volume discretization that uses multiple pressure degrees of freedoms to approximate the flux over the interface of two cells. The same discretization is used on the diffusive part of the transport in equations (7) and (8). The advective part is discretized by an upwind weighting. For the time derivative, we use the implicit second order Crank-Nicholson time stepping scheme. The resulting set of equations is nonlinear, and Newton’s method is used to solve it. The Jacobian of the system of equations is obtained by automatic differentiation [26]. Because the time scale of the dynamics between the fractures and rock matrix is in general large, we use an adaptive time-stepping that changes the time-step based on the convergence of Newton’s method.

The implementation is done in the open-source software PorePy [22], and we have validated our numerical method by comparing the initial fingering in a domain without fractures to linear stability analysis. The rock matrix is meshed by a logical Cartesian mesh conforming to the fractures. The 1d fracture meshes are matching the faces of the 2d mesh. The mixed-dimensional coupling between the fractures and rock matrix has been applied in PorePy for both flow and passive transport in several papers [32, 40, 18]. For postprocessing and visualization, Paraview has been applied [2]. To facilitate reproducibility, the run-scripts used in the simulations reported below are open sourced, see Berge et al. [4] for install instructions.

4 Results

Four different characteristic fracture networks are considered for the study of viscous fingering, illustrated in figure 2. All domains are periodic in the y - and x -direction, and the width of the domain, H , is restricted to either $H = W$ or $H = 2W$. As the length scale imposed by the fracture geometry coincide with the length scale imposed by the viscous fingers, we expect this choice of domain width to capture the periodic behavior of the system. We have performed numerical tests with wider domains to confirm that the solution in fact has a periodic behavior of width W . Note that if the distance between the fractures is smaller than the characteristic width of the viscous fingers (the length scale that enters in the Peclet number), there might be viscous fingering across the fracture geometry and a wider simulation domain is needed. Nijjer et al. [30] report similar behavior for layered porous media.

As a quantitative measure to compare solutions we use the mixing length $L_f(t)$. The mixing length is defined as the length of rock matrix $\hat{\Omega}_2$ where the two fluids have spread:

$$L_f(t) = \max(\hat{x}|_{c(\hat{x}, \hat{y}, t) > 0.9}) - \min(\hat{x}|_{c(\hat{x}, \hat{y}, t) < 0.1}) \quad \text{in } \hat{\Omega}_2. \quad (12)$$

In the following subsection, we present the simplest geometrical case of flow parallel to the fractures. We will vary each of the dimensionless numbers independently and study how this affect the viscous flow. This

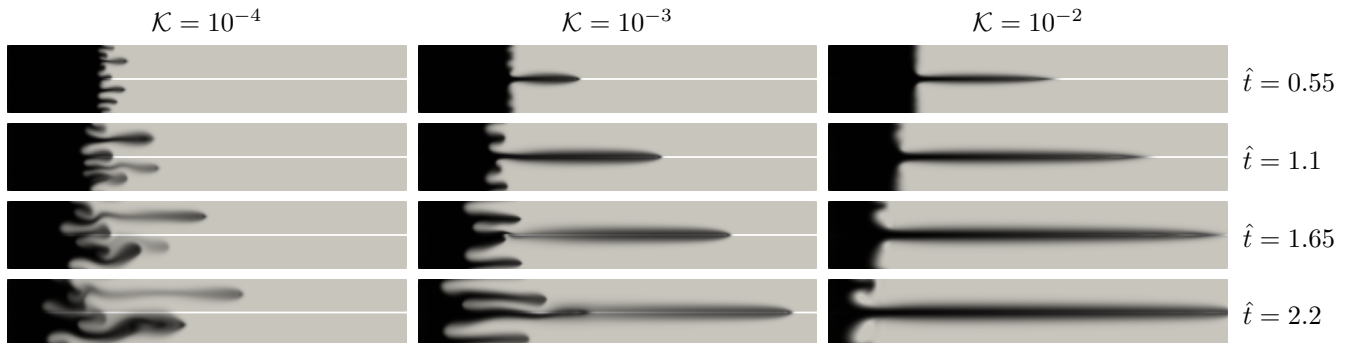


Figure 3: Domain with a fracture parallel to the flow direction. The figures show the time evolution of the concentration field for the parameters $(R, Pe, \mathcal{A}) = (3, 512, 10^{-4})$ and weighted permeability ratios $\mathcal{K} = 10^{-4}, 10^{-3}, 10^{-2}$. The simulations are plotted in a moving reference frame of dimensionless velocity 1.

will reveal important insight on the interplay between the viscous instabilities and the preferential flow paths through the fractures. In subsections 4.2 and 4.3, we change the fracture geometry and consider the brick fractures, the hexagon fractures and the rotated hexagon fractures [36]. The last subsection 4.4, is dedicated to comparing the mixing length of the different fracture geometries.

4.1 Parallel fractures

To understand the effect fractures have on viscous fingering, we first study the geometrically simple case of fractures parallel to the flow direction. In the following subsections we try to answer how the fractures affect the viscous fingering, and how they can change the flow patterns in rock matrix.

The simulations in this subsection are run in a moving frame of reference by a change of variables:

$$\tilde{x} = \hat{x} - \hat{t}, \quad \tilde{\mathbf{u}} = \hat{\mathbf{u}} - \mathbf{i},$$

where \mathbf{i} is the unit basis vector in the x -direction. The dimensionless size of the computational domain is set to $L/W = 6$ and $H/W = 1$, and the initial concentration jump is located at $S/W = 2$.

4.1.1 Influence of the weighted permeability ratio \mathcal{K}

To study the influence of the weighted permeability ratio \mathcal{K} defined in equation (9), we fix the Peclet number $Pe = 512$, the viscosity ratio $R = 3$, and the width ratio $\mathcal{A} = 10^{-4}$. The dimensionless numbers are defined in equation (11). Characteristic plots of the three different weighted permeability ratios $\mathcal{K} = 10^{-4}, 10^{-3}, 10^{-2}$ are shown in figure 3. When $\mathcal{K} = \mathcal{A}$ the advective transport in the fractures and in the rock matrix has approximately the same velocity, and the behavior of the system is qualitatively and quantitatively the same as for a case without any fractures. When the weighted permeability ratio is much larger than the width ratio, $\mathcal{K} \gg \mathcal{A}$, the fluid flow is completely dominated by the fracture network geometry. There is a single channel following the fracture, while the displacement front in the rock matrix is much more stable. For $\mathcal{K} > \mathcal{A}$ there is a transition region where the viscous instabilities compete with the fracture permeability ratio about deciding the flow pattern.

4.1.2 Influence of the width ratio \mathcal{A}

To study the influence of the width ratio, we fix the Peclet number $Pe = 512$, and the viscosity ratio $R = 3$. The weighted permeability ratio is fixed at the different values $\mathcal{K} = 10^{-3}, 10^{-2}, 10^{-1}$. For each of these values, the width ratio ranges from $\mathcal{A} = \mathcal{K}/100$ to $\mathcal{A} = \mathcal{K}$. The dimensionless numbers are defined in equation (11). Recall that the width ratio \mathcal{A} defines relative cross sectional area of the fracture and rock matrix, which indirectly defines the scaling of the advective velocity, \mathcal{K}/\mathcal{A} , in the fractures. If \mathcal{A} is large, there is a large volume in the fractures available for flow and the advection scaling \mathcal{K}/\mathcal{A} is close to one. If \mathcal{A} is small, there is a small volume available for flow, and the advective velocity in the fractures must be relatively higher for a fixed weighted permeability ratio.

The mixing length, L_f , for the cases $\mathcal{A} = \mathcal{K}$ is plotted in figure 4. For all weighted permeability ratios, the flow is in this case driven by the viscous instabilities and the quantitative measure does not differ much over the whole parameter range. For the highest weighted permeability ratio, $\mathcal{K} = 10^{-1}$, approximately ten percent of the fluid is flowing through the fractures. This extra volume seems to attract the fingers in the rock matrix towards the fractures which causes a slightly higher mixing length velocity.

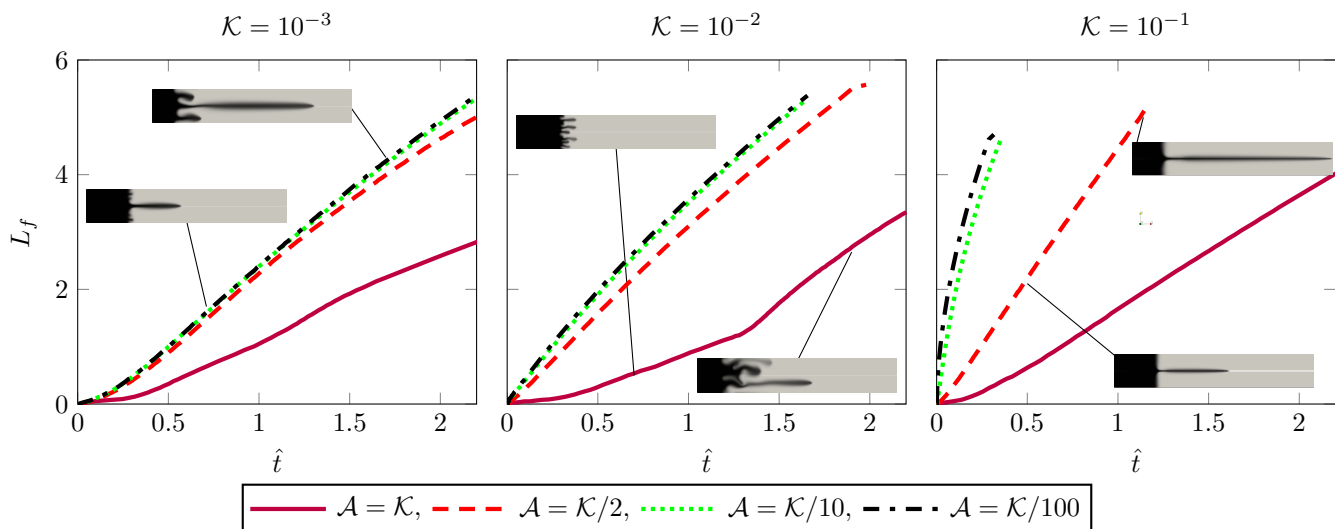


Figure 4: Domain with fractures parallel to the flow direction. The figures show the mixing length, L_f , for Péclet number $Pe = 512$ and viscosity ratio $R = 3$. Each plot shows a fixed weighted permeability ratio \mathcal{K} , and width ratios $\mathcal{A} = \mathcal{K}, \mathcal{K}/2, \mathcal{K}/10, \mathcal{K}/100$. When the fingers reach the end of the domain, the simulation is ended.

Even for a small decrease of the width ratio, $\mathcal{A} = \mathcal{K}/2$, the system changes character completely, as seen in figure 4. In this case the advective velocity in the fracture is approximately twice that of the velocity in the rock matrix. In all simulations, we observe a single finger aligned with the fracture that causes channeling through the domain. As the width ratio decreases further, $\mathcal{A} = \mathcal{K}/10$ (thus, the difference in advective velocity increases), it is only for the highest weighted permeability ratio, $\mathcal{K} = 10^{-1}$, there is a significant difference in the solution. For the smaller weighted permeability ratios $\mathcal{K} = 10^{-2}, 10^{-3}$ the increase of the advective scaling, \mathcal{K}/\mathcal{A} , in the fractures, does not increase the velocity of the mixing length. When the width ratio is reduced by another order of magnitude, $\mathcal{A} = \mathcal{K}/100$, there is not a significant change for any of the cases.

For the cases $\mathcal{A} < \mathcal{K}$, the maximum finger velocity is quickly reached as the width ratio \mathcal{A} decreases. After this point, the increase in the displacement front velocity in the fracture is counteracted by the diffusion and advection from the fracture to the rock matrix. The system does not change behavior when \mathcal{A} is changed further, and we can describe the effect of the fractures by only the weighted permeability ratio \mathcal{K} .

4.1.3 Reduction in number of fingers

In all simulations there are less fingers when $\mathcal{K} > \mathcal{A}$ (i.e., the scaling of the advective velocity in the fracture is larger than in the rock matrix $\mathcal{K}/\mathcal{A} > 1$) compared to the case $\mathcal{K} = \mathcal{A}$ (i.e., the scaling of the advective velocity is the same in the two domains $\mathcal{K}/\mathcal{A} = 1$), as can be seen in figures 3 and 4. Especially at early time steps the number of fingers in the rock matrix is greatly reduced, even for the smallest weighted permeability ratios \mathcal{K} .

This difference in the number of fingers is caused by an interaction of two interesting phenomena that occur due to the viscosity ratio and the permeability ratio. The viscous fingering is driven by pressure gradients, and when a finger is slightly ahead of its neighbors it will outrun them and shields them from further growth. Viscous shielding is also occurring for a homogeneous medium (see, e.g., Homsy [19]) and cannot alone cause the difference in the number of fingers. The second phenomena is a channeling effect through the fractures. Figure 5 shows the streamlines and pressure profile for a typical scenario. Initially, there is zero flow between the fracture and rock matrix. The advection is larger in the fracture than in the matrix because of the permeability difference, thus, the displacement front in the fracture moves faster. Due to the viscosity ratio, the faster displacement front causes a lower pressure in the fracture than in the rock matrix, which induces a flux from the rock matrix to the fracture. Upstream and downstream the volumetric flux ratio in the fracture and rock matrix is \mathcal{K} . Since the fluid is flowing from the rock matrix to the fracture at the displacement front in the rock matrix, it has to flow back out further downstream. This creates a channeling where the fluid flows from the matrix to the fracture at the displacement front in the rock matrix, is transported downstream the fracture, and flows back out in the matrix at the displacement front in the fracture. This process creates a finger aligned with the fracture. The channeling through the fracture in combination with the viscous shielding allows the finger aligned with the fracture to grow at a much higher rate than the fingers in the rock matrix. This stabilize the flow in the rock matrix; for the highest weighted permeability ratios, the displacement front does not show any sign of fingering.

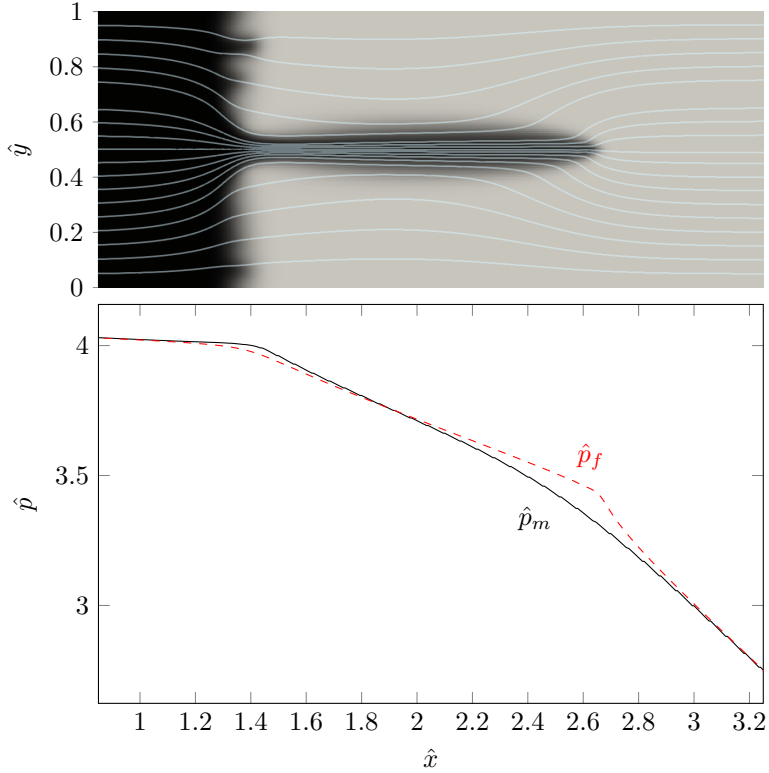


Figure 5: Typical streamlines for the flow through the parallel fracture network. The parameters are $(R, Pe, \mathcal{A}, \mathcal{K}) = (3, 512, 10^{-4}, 10^{-3})$. The bottom figure shows the pressure profile in the fracture (red dashes) and in the matrix for a plot over the line $\hat{y} = 0.9$ (solid black line).

4.2 Brick fractures

The brick fracture network (see figure 2) is anisotropic in the y - and x -axis. In this section we focus on flow in the x -axis. For flow in the y -axis the fractures going through the domain gives a behavior very similar to the previous case of fractures parallel to the flow. The brick fracture network is different from the parallel fracture network in two ways. First, all fractures are connected together by fractures parallel to the x -axis. Second, the fractures are broken in the x -axis, that is, there is no straight fracture that goes through the whole domain. We expect this to significantly alter the flow paths through the fracture network and rock matrix. For all simulations in this section we fix the Peclet number $Pe = 512$, viscosity ratio $R = 3$, and width ratio $\mathcal{A} = 10^{-3}$. The dimensionless size of the computational domain is set to $L/W = 6$ and $H/W = 2$, and the initial concentration jump is located at $S/W = 0$.

The first row of figure 6 shows the concentration field for the weighted permeability ratio $\mathcal{K} = 10^{-2}$. The pressure gradient due to the fractures is large enough to suppress the initial fingering, but at later times the viscous instabilities in the rock matrix grows large enough to cause fingering. The initial fingers of the fractures live through the simulation, but grows weaker towards the end. Compared to the same weighted permeability ratio for the parallel fracture (see figure 3) the flow is much more unstable.

The second row of figure 6 shows a higher weighted permeability ratio, $\mathcal{K} = 10^{-1}$. In this case we observe no viscous fingering, and the channeling through the domain is dominated by the fracture geometry. We observe an interesting effect when the injected fluid reaches the T-intersection of the brick fractures. The weighted permeability ratio is not so large that the fluid only follows the fracture network, but it takes a shortcut through the rock matrix. When the displacement front reaches the next fracture, the flow is again concentrated in the fracture. Finally, when the stable injection front in the rock matrix reaches the second pair of fractures aligned with the x -axis, it becomes favorable to flow through these fractures.

The last row of figure 6 shows a weighted permeability ratio of $\mathcal{K} = 1$. In this case, the flow patterns are completely defined by the fracture network. Initially, the flow is mainly channeled through the fracture network. Again, the trailing concentration front in the rock matrix is stable. Each vertical fracture acts as a line injection, but the concentration is reduced for each vertical fracture.

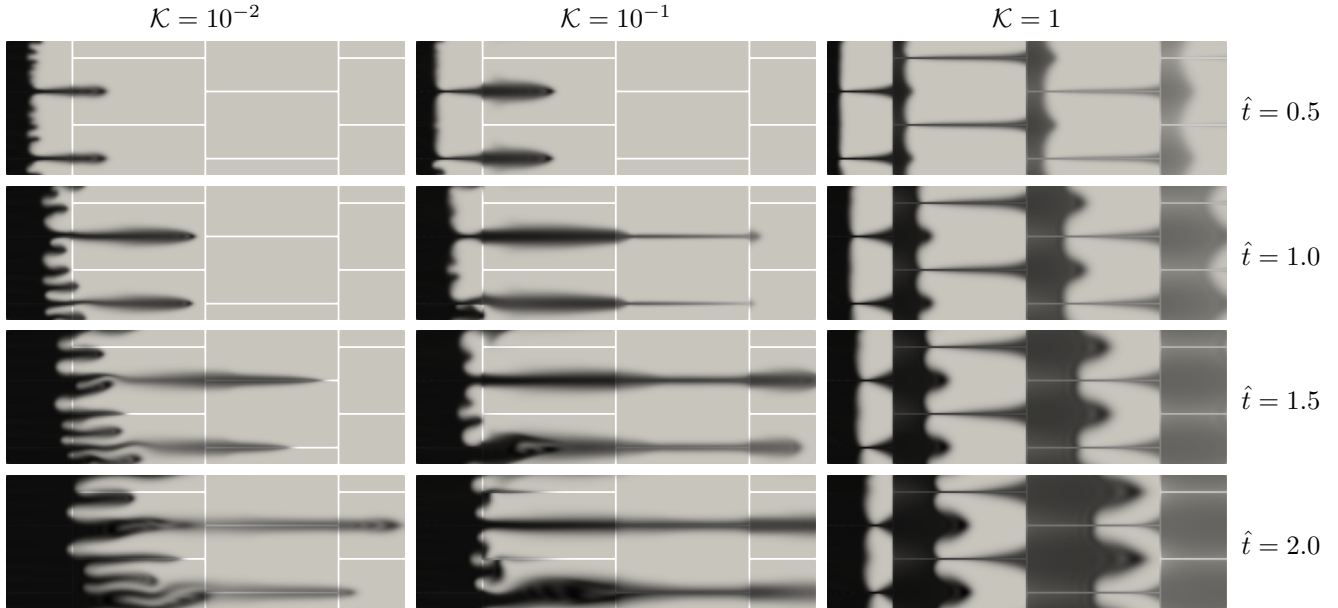


Figure 6: Time evolution of the concentration field for the brick fracture network. The parameters $(R, Pe, \mathcal{A}) = (3, 512, 10^{-3})$ are fixed, while the weighted permeability ratio is different for each simulation, $\mathcal{K} = 10^{-2}, 10^{-1}, 1$.

4.3 Hexagon fractures

In this section we consider the hexagonal fracture network (see figure 2). This network is similar to the brick network in that no fractures go straight through the domain in the flow direction. However, the fractures in y -axis are tilted, which makes it easier for the flow to go through them, and we expect that more fluid flow through the network compared to the brick network. For all simulations in this section we fix the Peclet number $Pe = 512$, viscosity ratio $R = 3$, and width ratio $\mathcal{A} = 10^{-3}$. The dimensionless size of the computational domain is set to $L/W = 10.5/\sqrt{3} \approx 6$ and $H/W = 2$, and the initial concentration jump is located at $S/W = 0$.

The first row of figure 7 shows the evolution of the displacement front for a small weighted permeability ratio $\mathcal{K} = 10^{-2}$. The fingers are predominantly following the fractures parallel to the x -axis, but when the fingers reach the tilted fractures they continue straight through the hexagon. We observe some unstable fingering in the rock matrix, but the fingers are mainly induced by the heterogeneities created by the fracture geometry.

The second row of figure 7 shows the displacement front for a weighted permeability ratio $\mathcal{K} = 10^{-1}$. The flow has a surprising behavior in this regime. In all previous cases we have studied the velocity of the finger length has increased with higher weighted permeability ratios. In this case, however, the fingers are shorter in the intermediate regime, $\mathcal{K} = 10^{-1}$, than for the smaller weighted permeability ratio $\mathcal{K} = 10^{-2}$. The reduction in mixing length can clearly be seen in figure 9. For the intermediate case of $\mathcal{K} = 10^{-1}$, the flow path through the fracture network is in balance with the shorter path straight through the hexagons. This creates two fingers inside each hexagon that trap parts of the higher viscous fluid in the middle. The trapped fluid then flows out through the next fracture parallel to the x -axis, which forces the viscous fingers to continue through the rock matrix parallel to the fractures.

The last row of figure 7 shows simulations for a high weighted permeability ratio $\mathcal{K} = 1$. The behavior is comparable to the brick case with the same weighted permeability ratio, shown in figure 6. First, the less viscous fluid is transported exclusively through the fracture network. The fluid is then transported from the fractures parallel to the x -axis to the rock matrix mainly by diffusion, while it is mainly transported by advection in the tilted fractures. The flow in the rock matrix is stable.

Figure 8 shows simulations for when the hexagon fracture network is rotated 90° . For this network there are no fractures parallel to the dominant flow direction. For the lower weighted permeability ratio $\mathcal{K} = 10^{-2}$, we observe some fingering in the rock matrix, but the set of fingers following the zig-zag fracture paths dominates. For the intermediate weighted permeability ratio $\mathcal{K} = 10^{-1}$, the fractures are dominating the flow. There is a tendency to a set of fingers between the fractures, but these never grows. The width of the fingers are comparable to the offset of the zig-zag fractures. For the high weighted permeability ratio $\mathcal{K} = 1$, there is first complete breakthrough of the viscous fluid in the fracture network before the displacement front in the matrix move significantly. At later times the flow pattern is similar to the intermediate regime, $\mathcal{K} = 10^{-1}$.

The hexagon fractures and rotated hexagon fractures represent the same fracture geometry, with orthogonal flow directions imposed. However, comparing the displacement fronts for the hexagon fractures in figure 7 with

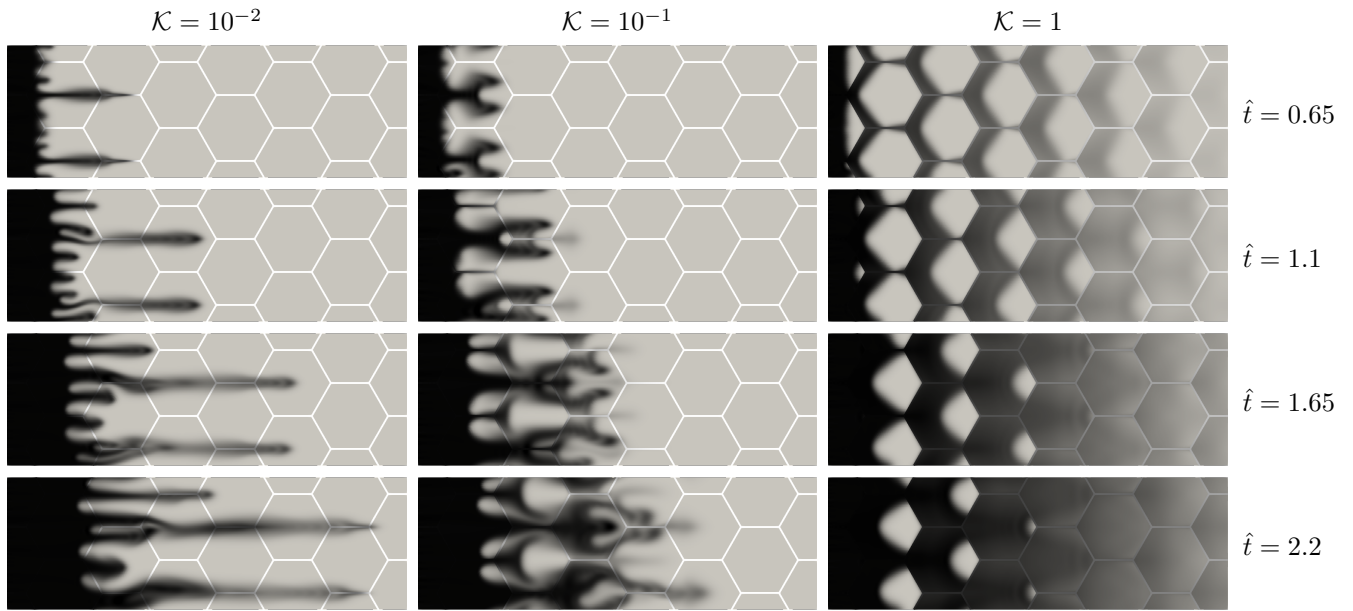


Figure 7: Time evolution of the concentration field for the hexagon fracture network. The parameters $(R, Pe, A) = (3, 512, 10^{-3})$ are fixed, while the weighted permeability ratio is different for each simulation, $\mathcal{K} = 10^{-2}, 10^{-1}, 1$.

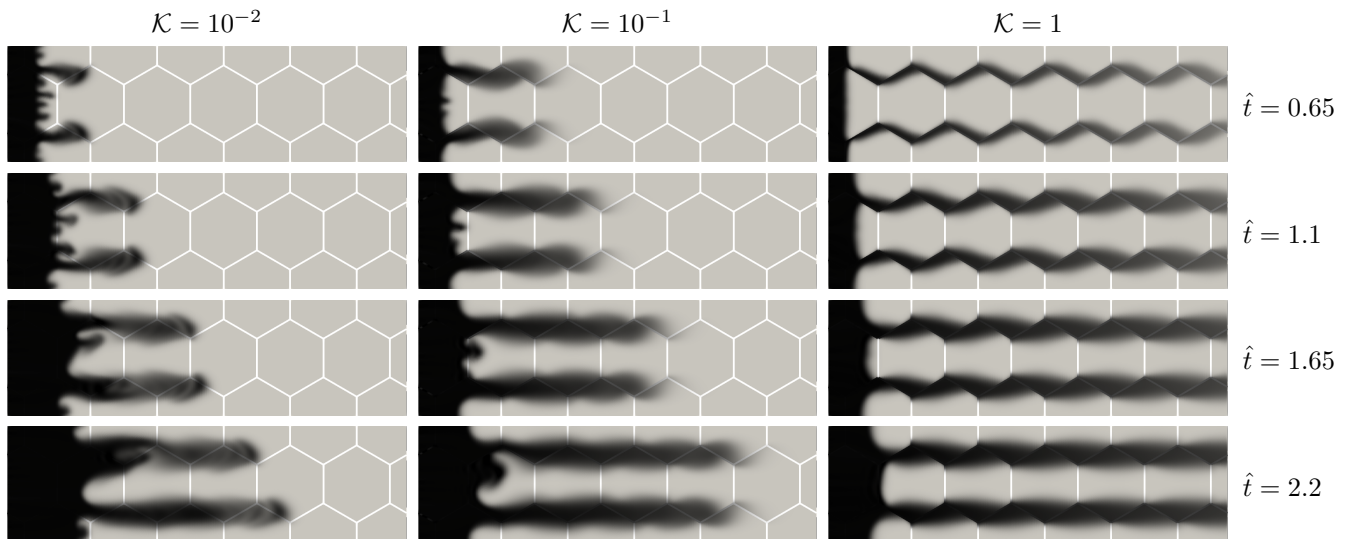


Figure 8: Time evolution of the concentration field for the rotated hexagon fracture network. The parameters $(R, Pe, A) = (3, 512, 10^{-3})$ are fixed, while the weighted permeability ratio is different for each simulation, $\mathcal{K} = 10^{-2}, 10^{-1}, 1$.

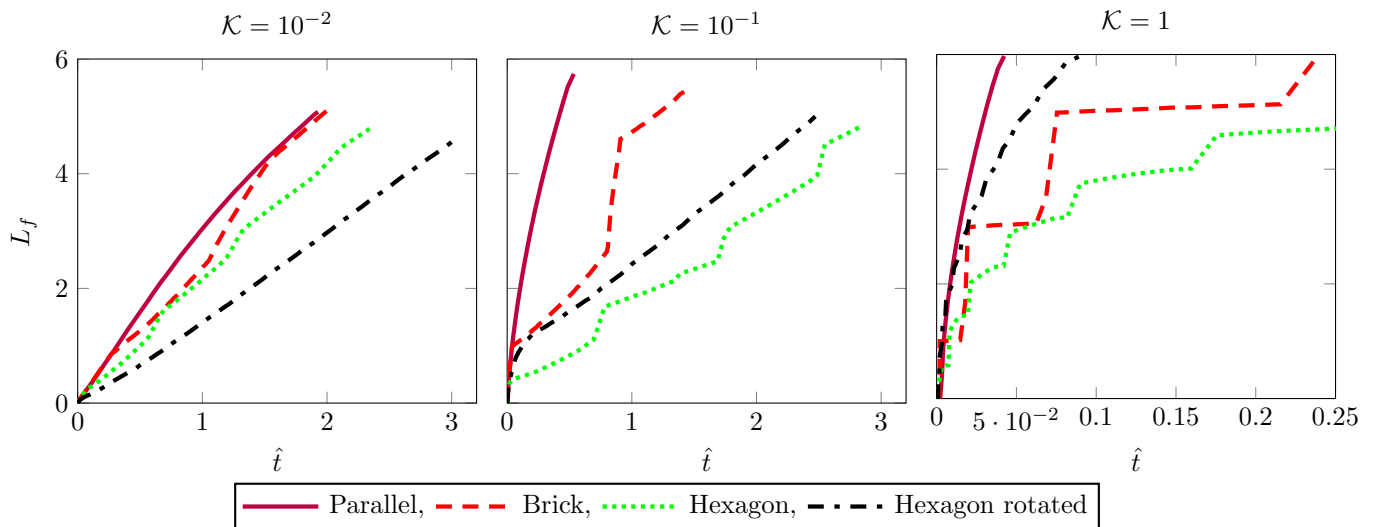


Figure 9: The figures show the mixing length, L_f , for the parallel fractures, brick, fractures, hexagon fractures and rotated hexagon fractures. The parameters $(R, Pe, A) = (3, 512, 10^{-3})$ are fixed, while the weighted permeability ratio is different for each figure, $\mathcal{K} = 10^{-2}, 10^{-1}, 1$. Note that the time scales of the plots are much smaller for the last case $\mathcal{K} = 1$.

the rotated hexagon fractures in figure 8, the flow paths through the two networks are fundamentally different. This demonstrate how the anisotropy of the fracture network is strongly enhanced by the non-linear flow. While we might fairly well understand unstable flow and fractured porous flow separately, the strong interaction between viscous instabilities and permeability ratios makes it challenging to understand the combined process.

4.4 Comparing mixing lengths of different geometries

Figure 9 shows the mixing length for each of the four fracture networks. For the lowest weighted permeability ratio, $\mathcal{K} = 10^{-2}$, the mixing length evolves similar for all geometries. However, the velocity of the mixing length differs significantly from the parallel fractures and the rotated hexagon fractures. For the parallel fractures, the viscous fingers follow the fracture to the end of the simulation. For the rotated hexagon fractures, the viscous fingers are not able to follow the zig-zag fractures, causing the fingers to spread over a wider domain in the rock matrix, which reduces the mixing length velocity.

For the intermediate weighted permeability ratio of $\mathcal{K} = 10^{-1}$, the initial mixing length velocity is approximately equal for all geometries. Except for the parallel fractures, the mixing length then slows down abruptly at different times for the different fracture networks. For both the brick network and the hexagon network the slowdowns are associated with the leading finger cutting straight through the rock matrix instead of following the fracture network (see figures 6 and 7). When the finger cutting through the rock matrix reaches the next fracture, the mixing length velocity speeds up again. The slowdown of the rotated hexagon fractures is due to the repeated kinks of the fractures, that cause the fluid to flow into the rock matrix. This is the same process as for the lower weighted permeability ratio $\mathcal{K} = 10^{-2}$, and the velocity after the slowdown is comparable in the two cases.

For the highest weighted permeability ratio, $\mathcal{K} = 1$, the fluid flow paths are completely given by the fracture geometries. The difference in mixing length between the geometries is given by how far the fluid has to travel through the fracture network. We observe a slowdown of the mixing length velocities because of two different phenomena. For the brick and hexagon fractures, a distinct slowdown is associated with the displacement front traveling through a fracture aligned predominantly in the y -axis. When the displacement front reaches a fracture aligned with the x -axis, the mixing length velocity increases again. This creates the clear oscillation in the mixing lengths for the brick and hexagon networks. There is also a more gradual slowdown for all fracture networks. We believe this is caused by a dilution of the viscous fingers as they travel downstream. When the concentration decreases, so does the fluid flux due to a corresponding change in viscosity. The dilution can clearly be seen in figures 6 and 7 for the brick and hexagon networks. Towards the end of the simulations, boundary effects probably also effect the results.

5 Conclusion

In this paper we use numerical simulations to study the effect fractures have on miscible viscous fingering in porous media. From the non-dimensionalization of the equations, two new dimensionless numbers are derived. The first dimensionless number is the width ratio between the aperture and the longitudinal separation of the fractures. The second is a weighted ratio between the permeability of the fractures and the permeability of the rock matrix. The numerical simulations show that it is the weighted permeability ratio that is most important in describing the effect the fracture network has on the fluid flow. As the weighted permeability ratio increases, we demonstrate how there is a transition from a viscous fingering regime to a regime where the preferential flow paths are given by the fracture network. The exact transition depends on the geometry of the fracture network. For the geometries considered in this paper the transition takes place when the weighted permeability ratio is one to two orders of magnitude larger than the width ratio.

The permeability contrast between the rock matrix and fractures is essential for the viscous fingering; regimes that are viscously unstable for a homogeneous porous medium, might be stable if fractures are added. When there is a permeability contrast between the fractures and rock matrix, fingers aligned with the fractures always form. The fingers initiated by the fractures quickly outgrow the viscous fingers in the rock matrix, even at modest permeability contrasts. The fingers aligned with the fractures greatly shield the viscous fingering in the rock matrix and stabilizes the initial fingering process. When the permeability contrast is sufficiently large, the displacement front in the rock matrix is stable and only channeling along the fractures is observed. In these cases the flow paths are completely given by the fracture network.

A new phenomenon is observed for the viscous flow in a domain with highly permeable fractures. Because of the permeability contrast, the displacement front in the fractures moves faster than the displacement front in the rock matrix. In combination with viscosity effects, this causes a flux from the rock matrix to the fractures around the displacement front in the rock matrix. The less viscous fluid is then transported downstream in the fracture until it reaches the displacement front in the fracture, where the fluid flows back to the rock matrix. At the displacement front in the rock matrix this induces a pressure gradient towards the fractures, which may be larger than the pressure gradient created by the viscous instabilities.

Several different fracture network geometries is considered in this paper. All geometries show the same transition from unstable flow to flow dominated by the fractures as the permeability contrast increased. However, the interaction between the viscous instabilities and fracture geometry leads to fundamentally different flow paths through the different porous media. We find that the geometry is especially important at the transition from the viscously unstable regime to the regime dominated by the fracture network. In the transition regime, the preferential flow paths created by the viscous fingers are of the same order as the fixed flow paths through the fracture network, which allows the viscous instabilities in the rock matrix to grow. As time evolves, a few of the fingers in the rock matrix can grow large enough to compete with the channeling along the fractures.

In sum, the examples in this paper show the complex interplay between fracture geometry and unstable flow. The strong geometry dependency gives an important lesson in terms of quantification and upscaling of flow and mixing: While clear fracture flow and viscous fingering regimes can be identified, there are important cross-over regimes where classical a priori assumptions on the fluid flow structure fail.

References

- [1] I. Aavatsmark. An introduction to multipoint flux approximations for quadrilateral grids. *Computational Geosciences*, 6(3):405–432, Sept. 2002. ISSN 1573-1499. doi: 10.1023/A:1021291114475. URL <https://doi.org/10.1023/A:1021291114475>.
- [2] U. Ayachit. *The ParaView Guide: A Parallel Visualization Application*. Kitware, Inc., USA, 2015. ISBN 1930934300, 9781930934306.
- [3] J.-C. Bacri, N. Rakotomalala, D. Salin, and R. Wouméni. Miscible viscous fingering: Experiments versus continuum approach. *Physics of Fluids A: Fluid Dynamics*, 4(8):1611–1619, 1992. doi: 10.1063/1.858383. URL <https://doi.org/10.1063/1.858383>.
- [4] R. L. Berge, I. Berre, E. Keilegavlen, and J. M. Nordbotten. Viscous fingering in fractured porous media. Zenodo. doi: 10.5281/zenodo.3249931, June 2019.
- [5] R. L. Berge, Ø. S. Klemetsdal, and K.-A. Lie. Unstructured voronoi grids conforming to lower dimensional objects. *Computational Geosciences*, 23(1):169–188, Feb. 2019. ISSN 1573-1499. doi: 10.1007/s10596-018-9790-0. URL <https://doi.org/10.1007/s10596-018-9790-0>.
- [6] B. Berkowitz. Characterizing flow and transport in fractured geological media: A review. *Advances in Water Resources*, 25(8):861–884, 2002. ISSN 0309-1708. doi: 10.1016/S0309-1708(02)00042-8. URL <http://www.sciencedirect.com/science/article/pii/S0309170802000428>.

- [7] I. Berre, F. Doster, and E. Keilegavlen. Flow in fractured porous media: A review of conceptual models and discretization approaches. *Transport in Porous Media*, Oct. 2018. ISSN 1573-1634. doi: 10.1007/s11242-018-1171-6. URL <https://doi.org/10.1007/s11242-018-1171-6>.
- [8] M. A. Christie. High-resolution simulation of unstable flows in porous media. *SPE Reservoir Engineering*, 4(03):297–303, 1989. doi: 10.2118/16005-PA. URL <https://doi.org/10.2118/16005-PA>.
- [9] J. Y. Y. Chui, P. de Anna, and R. Juanes. Interface evolution during radial miscible viscous fingering. *Phys. Rev. E*, 92:041003, Oct. 2015. doi: 10.1103/PhysRevE.92.041003. URL <https://link.aps.org/doi/10.1103/PhysRevE.92.041003>.
- [10] A. De Wit. Miscible density fingering of chemical fronts in porous media: Nonlinear simulations. *Physics of Fluids*, 16(1):163–175, 2004. doi: 10.1063/1.1630576. URL <https://doi.org/10.1063/1.1630576>.
- [11] A. De Wit and G. M. Homsy. Viscous fingering in periodically heterogeneous porous media. I. Formulation and linear instability. *The Journal of Chemical Physics*, 107(22):9609–9618, 1997. doi: 10.1063/1.475258. URL <https://doi.org/10.1063/1.475258>.
- [12] A. De Wit and G. M. Homsy. Viscous fingering in periodically heterogeneous porous media. II. Numerical simulations. *The Journal of Chemical Physics*, 107(22):9619–9628, 1997. doi: 10.1063/1.475259. URL <https://doi.org/10.1063/1.475259>.
- [13] P. Dietrich, R. Helmig, M. Sauter, H. Hötzl, J. Köngeter, and G. Teutsch. *Flow and Transport in Fractured Porous Media*. Springer, Berlin, Heidelberg, 2005. doi: 10.1007/b138453.
- [14] M. T. Elenius and K. Johannsen. On the time scales of nonlinear instability in miscible displacement porous media flow. *Computational Geosciences*, 16(4):901–911, Sept. 2012. ISSN 1573-1499. doi: 10.1007/s10596-012-9294-2. URL <https://doi.org/10.1007/s10596-012-9294-2>.
- [15] M. T. Elenius, J. M. Nordbotten, and H. Kalisch. Convective mixing influenced by the capillary transition zone. *Computational Geosciences*, 18(3):417–431, Aug. 2014. ISSN 1573-1499. doi: 10.1007/s10596-014-9415-1. URL <https://doi.org/10.1007/s10596-014-9415-1>.
- [16] B. Flemisch, I. Berre, W. Boon, A. Fumagalli, N. Schwenck, A. Scotti, I. Stefansson, and A. Tatomir. Benchmarks for single-phase flow in fractured porous media. *Advances in Water Resources*, 111:239–258, 2018. ISSN 0309-1708. doi: <https://doi.org/10.1016/j.advwatres.2017.10.036>. URL <http://www.sciencedirect.com/science/article/pii/S0309170817300143>.
- [17] X. Fu, L. Cueto-Felgueroso, and R. Juanes. Viscous fingering with partially miscible fluids. *Phys. Rev. Fluids*, 2:104001, Oct. 2017. doi: 10.1103/PhysRevFluids.2.104001. URL <https://link.aps.org/doi/10.1103/PhysRevFluids.2.104001>.
- [18] A. Fumagalli and E. Keilegavlen. Dual virtual element methods for discrete fracture matrix models. *Oil and Gas Science and Technology*, 74, 11 2019. doi: 10.2516/ogst/2019008. URL <https://doi.org/10.2516/ogst/2019008>.
- [19] G. M. Homsy. Viscous fingering in porous media. *Annual Review of Fluid Mechanics*, 19(1):271–311, 1987. doi: 10.1146/annurev.fl.19.010187.001415. URL <https://doi.org/10.1146/annurev.fl.19.010187.001415>.
- [20] B. Jha, L. Cueto-Felgueroso, and R. Juanes. Quantifying mixing in viscously unstable porous media flows. *Phys. Rev. E*, 84:066312, Dec. 2011. doi: 10.1103/PhysRevE.84.066312. URL <https://link.aps.org/doi/10.1103/PhysRevE.84.066312>.
- [21] M. Karimi-Fard, L. J. Durlofsky, and K. Aziz. An efficient discrete fracture model applicable for general purpose reservoir simulators. *Society of petroleum engineers*, 2003. doi: 10.2118/79699-MS. SPE Reservoir Simulation Symposium, 3-5 February, Houston, Texas.
- [22] E. Keilegavlen, A. Fumagalli, R. L. Berge, I. Stefansson, and I. Berre. Porepy: An open-source simulation tool for flow and transport in deformable fractured rocks, 2017. URL <http://arxiv.org/abs/1712.00460>.
- [23] A. R. Kopf-Sill and G. M. Homsy. Nonlinear unstable viscous fingers in Hele-Shaw flows. I. Experiments. *The Physics of Fluids*, 31(2):242–249, 1988. doi: 10.1063/1.866854. URL <https://aip.scitation.org/doi/abs/10.1063/1.866854>.
- [24] O. Manickam and G. M. Homsy. Fingering instabilities in vertical miscible displacement flows in porous media. *Journal of Fluid Mechanics*, 288:75–102, 1995. doi: 10.1017/S0022112095001078.

- [25] V. Martin, J. Jaffr, and J. Roberts. Modeling fractures and barriers as interfaces for flow in porous media. *SIAM Journal on Scientific Computing*, 26(5):1667–1691, 2005. doi: 10.1137/S1064827503429363. URL <https://doi.org/10.1137/S1064827503429363>.
- [26] U. Naumann. *The Art of Differentiating Computer Programs: An Introduction to Algorithmic Differentiation*. Number 24 in Software, Environments, and Tools. SIAM, Philadelphia, PA, 2012. ISBN 978–1–611972–06–1. URL <http://bookstore.siam.org/se24>.
- [27] S. P. Neuman. Trends, prospects and challenges in quantifying flow and transport through fractured rocks. *Hydrogeology Journal*, 13(1):124–147, Mar. 2005. ISSN 1435-0157. doi: 10.1007/s10040-004-0397-2. URL <https://doi.org/10.1007/s10040-004-0397-2>.
- [28] C. Nicolaidis, B. Jha, L. Cueto-Felgueroso, and R. Juanes. Impact of viscous fingering and permeability heterogeneity on fluid mixing in porous media. *Water Resources Research*, 51(4):2634–2647, 2015. doi: 10.1002/2014WR015811. URL <https://agupubs.onlinelibrary.wiley.com/doi/abs/10.1002/2014WR015811>.
- [29] J. S. Nijjer, D. R. Hewitt, and J. A. Neufeld. The dynamics of miscible viscous fingering from onset to shutdown. *Journal of Fluid Mechanics*, 837:520–545, 2018. doi: 10.1017/jfm.2017.829. URL <https://doi.org/10.1017/jfm.2017.829>.
- [30] J. S. Nijjer, D. R. Hewitt, and J. A. Neufeld. Stable and unstable miscible displacements in layered porous media. *Journal of Fluid Mechanics*, 869:468–499, 2019. doi: 10.1017/jfm.2019.190. URL <https://doi.org/10.1017/jfm.2019.190>.
- [31] A. Nissen, E. Keilegavlen, T. H. Sandve, I. Berre, and J. M. Nordbotten. Heterogeneity preserving upscaling for heat transport in fractured geothermal reservoirs. *Computational Geosciences*, 22(2):451–467, Apr. 2018. ISSN 1573-1499. doi: 10.1007/s10596-017-9704-6. URL <https://doi.org/10.1007/s10596-017-9704-6>.
- [32] J. M. Nordbotten, W. M. Boon, A. Fumagalli, and E. Keilegavlen. Unified approach to discretization of flow in fractured porous media. *Computational Geosciences*, 23(2):225–237, Apr. 2019. ISSN 1573-1499. doi: 10.1007/s10596-018-9778-9. URL <https://doi.org/10.1007/s10596-018-9778-9>.
- [33] P. Petitjeans, C.-Y. Chen, E. Meiburg, and T. Maxworthy. Miscible quarter five-spot displacements in a hele-shaw cell and the role of flow-induced dispersion. *Physics of Fluids*, 11(7):1705–1716, 1999. doi: 10.1063/1.870037. URL <https://doi.org/10.1063/1.870037>.
- [34] V. Reichenberger, H. Jakobs, P. Bastian, and R. Helmig. A mixed-dimensional finite volume method for two-phase flow in fractured porous media. *Advances in Water Resources*, 29(7):1020–1036, 2006. ISSN 0309-1708. doi: <https://doi.org/10.1016/j.advwatres.2005.09.001>. URL <http://www.sciencedirect.com/science/article/pii/S0309170805002150>.
- [35] A. Riaz, M. Hesse, H. A. Tchelepi, and F. M. Orr. Onset of convection in a gravitationally unstable diffusive boundary layer in porous media. *Journal of Fluid Mechanics*, 548:87–111, 2006. doi: 10.1017/S0022112005007494.
- [36] P. N. Sævik and C. W. Nixon. Inclusion of topological measurements into analytic estimates of effective permeability in fractured media. *Water Resources Research*, 53(11):9424–9443, 2017. doi: 10.1002/2017WR020943. URL <https://agupubs.onlinelibrary.wiley.com/doi/abs/10.1002/2017WR020943>.
- [37] M. Sahimi. *Flow and Transport in Porous Media and Fractured Rock: From Classical Methods to Modern Approaches*. John Wiley and Sons, 2011. ISBN 9783527636693. doi: 10.1002/9783527636693.
- [38] M. Sajjadi and J. Azaiez. Scaling and unified characterization of flow instabilities in layered heterogeneous porous media. *Phys. Rev. E*, 88:033017, Sept. 2013. doi: 10.1103/PhysRevE.88.033017. URL <https://link.aps.org/doi/10.1103/PhysRevE.88.033017>.
- [39] M. R. Shahnazari, I. Maleka Ashtiani, and A. Saberi. Linear stability analysis and nonlinear simulation of the channeling effect on viscous fingering instability in miscible displacement. *Physics of Fluids*, 30(3):034106, 2018. doi: 10.1063/1.5019723. URL <https://doi.org/10.1063/1.5019723>.
- [40] I. Stefansson, I. Berre, and E. Keilegavlen. Finite-volume discretisations for flow in fractured porous media. *Transport in Porous Media*, 124(2):439–462, Sept. 2018. ISSN 1573-1634. doi: 10.1007/s11242-018-1077-3. URL <https://doi.org/10.1007/s11242-018-1077-3>.
- [41] C. T. Tan and G. M. Homsy. Stability of miscible displacements in porous media: Rectilinear flow. *The Physics of Fluids*, 29(11):3549–3556, 1986. doi: 10.1063/1.865832. URL <https://aip.scitation.org/doi/abs/10.1063/1.865832>.

- [42] C. T. Tan and G. M. Homsy. Stability of miscible displacements in porous media: Radial source flow. *The Physics of Fluids*, 30(5):1239–1245, 1987. doi: 10.1063/1.866289. URL <https://aip.scitation.org/doi/abs/10.1063/1.866289>.
- [43] Y. C. Yortsos and M. Zeybek. Dispersion driven instability in miscible displacement in porous media. *The Physics of Fluids*, 31(12):3511–3518, 1988. doi: 10.1063/1.866918. URL <https://aip.scitation.org/doi/abs/10.1063/1.866918>.
- [44] W. B. Zimmerman and G. M. Homsy. Nonlinear viscous fingering in miscible displacement with anisotropic dispersion. *Physics of Fluids A: Fluid Dynamics*, 3(8):1859–1872, 1991. doi: 10.1063/1.857916. URL <https://doi.org/10.1063/1.857916>.
- [45] W. B. Zimmerman and G. M. Homsy. Viscous fingering in miscible displacements: Unification of effects of viscosity contrast, anisotropic dispersion, and velocity dependence of dispersion on nonlinear finger propagation. *Physics of Fluids A: Fluid Dynamics*, 4(11):2348–2359, 1992. doi: 10.1063/1.858476. URL <https://doi.org/10.1063/1.858476>.